Exploring Q-scatter in Kinetic Inductance Detectors

To obtain the degree of Bachelor of Science
at the Delft University of Technology

by

Maxim Herman

To be defended publicly on
July 4th, 2025 at 10:00

Studentnumber:	5840937
Project duration:	22 April 2025 – 4 July 2025
Daily supervisor:	PhD Candidate Wilbert G. Ras
Thesis committee:	Prof.Dr.Ir Jochem J.A. Baselmans, TU Delft (Supervisor)
	Dr. Pieter J. de Visser, SRON (Supervisor)
	Dr. Iman E. Zadeh, TU Delft

TU Delft

Abstract

Superconducting kinetic inductance detectors will play an important role in the future of exoplanet spectroscopy. Their low bandgap and the possibillity that they can be multiplexed into large arrays open up new opportunities where conventional semiconductors stop. A key requirement for the performance of these new detectors is the consistency of their quality factor (Q-factor). Variations in Q-factors, known as Q-scatter, result in nonuniform sensitivity and hold back scaling to larger systems.

In this thesis, detectors that differ in fabrication, pixel count and pixel spacing are analyzed and compared to find out what is the cause of Q-scatter. Possible causes include design errors, inaccurate fabrication, electromagnetic crosstalk, magnetic vortices and unbalanced transmission lines. Analysis showed Q-scatter is unlikely to be impacted by design, fabrication method, electromagnetic coupling or vortex forming. Also, no spatial relations, that indicated any transmission line effects, were observed. What is interesting however, is that the Q-factors of one of the chips seem to scatter all over again when measuring the chip again after trimming one of its components.

With the data available in this experiment it was not possible to give an concrete cause of Q-scatter. Furhter experiments, especially concerning the new scattering need to be conducted. Also, simulations using Sonnet v19 can give more insights in the origin of Q-scatter.

Contents

1 Introduction 4
1.1 Exoplanet spectroscopy . . . 4
1.2 Superconducting detectors . . . 4
1.3 Q-scatter . . . 6

2 Theory 7
2.1 Microwave resonators . . . 7
2.2 Superconductivity . . . 7
2.3 Array design and frequency multiplexing . . . 8
2.4 Q-scatter . . . 9
2.4.1 Q-factor . . . 9
2.4.2 Transmission . . . 10
2.4.3 Scatter . . . 11

3 Method 13
3.1 Fabrication . . . 13
3.2 KID devices . . . 14
3.3 Cryogenic measurement setup . . . 16
3.4 Measuring and mapping Q . . . 16
3.5 Power . . . 17

4 Results and discussion 19
4.1 Scatter . . . 20
4.1.1 Spatial dependence . . . 22
4.2 Correlations . . . 23
4.3 Trim comparison . . . 26

5 Conclusion 29

6 Appendix 31

Chapter 1

Introduction

The search for extraterrestrial life has inspired decades of astronomical research. A critical component of this search is the detection and characterization of exoplanets, planets outside our solar system that may harbor conditions suitable for life. Upcoming projects, such as the European Extremely Large Telescope and the Habitable Worlds Observatory, will require advanced photon detection systems to carry out precision spectroscopy on distant planetary atmospheres.

1.1 Exoplanet spectroscopy

To assess the potential for life on an exoplanet, astronomers search for biomarkers, molecules that indicate biological activity. Gases such as water vapor, carbon dioxide, and methane are key examples of these biomarkers. To determine which gasses are present in the atmosphere of an exoplanet that is lightyears away we use spectroscopy. Spectroscopy is based on the ability of light to be absorbed and emitted by atoms and molecules, leaving characteristic spectral fingerprints. These patterns differ for every atom or molecule and form the basis of spectroscopy. Gasses present in the atmosphere of an exoplanet can be identified by analyzing their atmospheric spectra. Key biomarkers such as water vapor, carbon dioxide, and methane each absorb light at specific wavelengths, primarily in the visible and near-infrared (VIS-NIR) part of the spectrum. However, the light that passes through the atmosphere of an exoplanet is extremely faint, down to a single photon per second hitting the detector.

1.2 Superconducting detectors

Conventional semiconductor detectors are limited in their ability to detect single photons. The bandgap of such a semiconductor has a magnitude for which a single photon in the visible range can only excite one electron to the conduction band. Most semiconductor detectors are based on silicon (Si) which has a bandgap of about 1.1 eV, an energy equal to a photon with a wavelength of

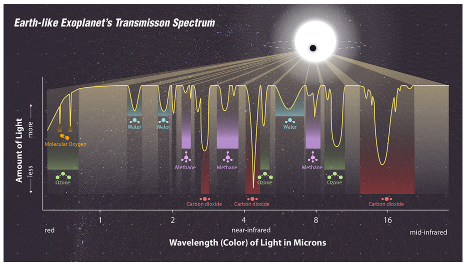

Figure 1.1: The transmission specturm of an Earth-like exoplanet. As the light passes through the atmosphere light gets absorbed by molecules present in the atmosphere, this causes the dips in the spectrum. Each molecule has its own characteristic dips. The dips of these molecules lie in the visible/near-infrared range of the spectrum.[1]

around 1.1 µm [8]. Visible photons thus do have sufficient energy to generate an electron-hole pair, but each photon generally creates only one charge carrier. As a result, these detectors cannot directly measure photon energy or distinguish between photons of different wavelengths without additional optics.

This limitation can be overcome through the use of superconducting materials. Superconductors form so-called Cooper pairs below their critical temperature, near absolute zero. These Cooper pairs have a bandgap Δ that is about a thousand times lower than the energy carried by VIS-NIR photons. Therefore, a VIS-NIR photon with an energy of $\hbar\omega > 2\Delta$ can brake about a thousand Cooper pairs depending on its exact energy, creating two quasiparticles for every Cooper pair. This makes a superconducting detector extremely sensitive compared to semiconductor detectors where a photon can only excite one electron[4]. This principle is used to make so-called KIDs, the detectors relevant to this thesis.

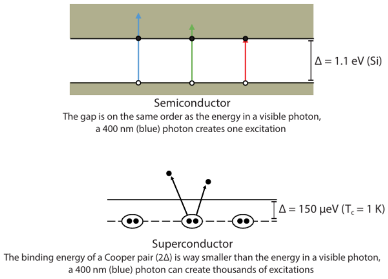

Figure 1.2: Where a VIS-NIR photon has just enough energy to overcome the bandgap Δ for a semiconductor, it has enough energy to break thousands of Cooper pairs in a superconductor. The energy needed to break a Cooper pair is 2Δ[8].

1.3 Q-scatter

A crucial factor in the performance of KIDs is their quality factor, or Q-factor, which determines how efficiently they can store and respond to energy. Generally, KIDs have high Q-factors to make them highly responsive to absorbed photons. KIDs in this thesis were designed to have a Q-factor of $5 \cdot 10^4$. However, in practice, significant variation is observed in the measured Q-factors across the array. This phenomenon, referred to as Q-scatter, possibly arises due to design errors, imperfections in fabrication, electromagnetic coupling between KIDs, magnetic vortices or unbalanced tranmission lines. This list is not exhaustive and causes can be excluded or added in future research. With wildly varying Q-factors, the KID responses will be non-uniform as the sensitivity can vary from pixel to pixel. Also, a consistent Q-factor allows for a higher multiplexing density in the array allowing to scale to larger systems.

This thesis, written to obtain a Bachelor of Science in Applied Physics at Delft University of Technology, focuses on investigating the origins and behavior of Q-scatter in KIDs and how it can be minimized. Chapter 2 will give the necessary theoretical background, followed by the methodology in chapter 3. In chapter 4 the results will be discussed and the findings will be concluded in chapter 5.

Chapter 2

Theory

The detectors that are relevant to this thesis consist of multiple so-called KIDs. KID stands for 'kinetic inductance detector', at the end of this theory section you will have idea why it is called this way. KIDs can all be connected to the same transmission line forming a large array that can be designed as a chip.

2.1 Microwave resonators

Each KID can be modeled as an LC resonator, consisting of a superconducting photosensitive inductor and a capacitor. The resonance frequency f_0 of such a circuit is determined by eq. (2.1), where L is the inductance and C the total capacitance. At this frequency, energy oscillates between the electric field in the capacitor and the magnetic field in the inductor.

$$f_0 = \frac{1}{2\pi\sqrt{LC}}, \tag{2.1}$$

The capacitance consists of an interdigitated capacitor (IDC), a finger-like capacitor made from NbTiN. Together with the inductor, made from the superconductor β-Ta, they are capacitively coupled to the transmission line, as can be seen in figure 2.1.

2.2 Superconductivity

The inductor of a KID is the part that makes it sensitive to light. β-Ta is a disordered superconductor with a high impedance, matching relatively good to free space compared to commonly used superconductors like aluminum. This gives the inductor an absorption efficiency of 30 % to 50% in the VIS-NIR range, an extensive analysis on photon-yield is made in Ref. [7].

When a photon hits, Cooper pairs are broken and quasiparticles are formed. The increase in the quasiparticle density is the central process in a KID. The

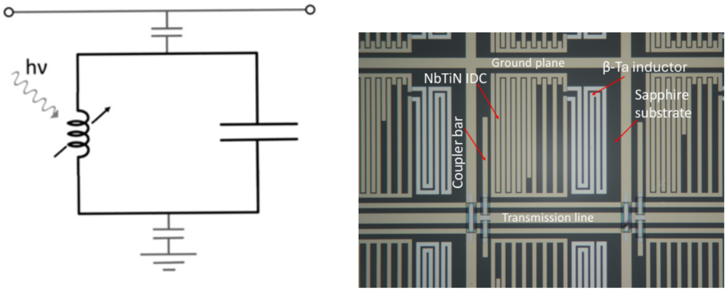

Figure 2.1: (Left) A schematic representation of an LC-circuit representing a KID. (Right) A KID as seen from under an optical microscope [11].

density of the quasiparticles is what influences the complex conductivity, which then ultimately changes the kinetic inductance.

The complex conductivity for a superconductor is given by:

$$\sigma(\omega) = \sigma_1(\omega) - i\sigma_2(\omega) \tag{2.2}$$

where σ_1 is the conductivity for electrons in a normal state and σ_2 the conductivity for electrons in a superconducting state. Expressions for these conductivities can be found using the Drude model[8].
The Cooper pairs do not feel resistance and thus do not dissipate energy. However, these electrons do have mass, meaning they have a delayed response to a change of electric field. Since this inductive behavior is coupled to the inertia of electrons, it is referred to as kinetic inductance, hence the name of the detectors. An increase in quasiparticle density increases $\sigma_1(\omega)$ resulting in more dissipative loss and thus a lower Q-factor. Further, it lowers $\sigma_2(\omega)$ and since this is inversely proportional with the kinetic inductance a decrease in $\sigma_2(\omega)$ corresponds to an increase in kinetic inductance. Since the resonance frequency is dependent on the inductance with an inverse square, the resonance frequency will go down when a photon is absorbed by the detector[8].

2.3 Array design and frequency multiplexing

In order to have a practical, working detector multiple KIDs need to be combined into a single array. This is possible by the fact that the capacitor or inductor in each KID can be slightly changed, resulting in KIDs with different resonance frequencies. This enables frequency multiplexing: multiple KIDs can be coupled to a single transmission line and be read out simultaneously. However, there is a limit to the number of KIDs that can be placed on a certain bandwidth. As more KIDs are placed on an array the spacing between resonance frequencies inevitably decreases. To avoid overlap between resonances, frequencies are designed to have uniform spacing between them. The frequencies for each KID

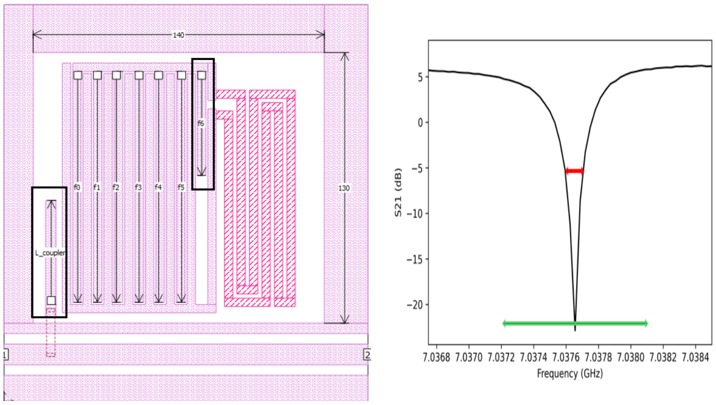

Figure 2.2: (Left) The design for the KIDs, circled in the left is the couplar bar with length $L_{coupler}$ and cirkled in the right is one of the IDC-fingers with length f6. (Right) An example of a transmission dip.

can be shifted by changing the length of the IDC-finger f6 as can be seen in the left picture in figure 2.2. Changing this length corresponds to the green arrow in the figure on the right. The red arrow indicates how the Q-factor changes as the length of the coupler bar is varied and will further discussed in section 3.2.

Nevertheless, in Ref. [11] it is observed there are big differences in frequency spacing. The error in measured resonance frequencies compared to designed resonance frequencies is called frequency scatter. This frequency scatter, investigated in Ref. [11], is minimized by trimming the IDC fingers in an additional fabrication step using electron beam lithography, which is further discussed in the next chapter. Another requirement for high multiplexing factors are narrow resonance frequency dips, so that the resonances are less likely to overlap. Narrow dips will require high Q-factors as we will see in the next section.

2.4 Q-scatter

2.4.1 Q-factor

A KID attenuates the signal send through the transmission line when it has the correct associated resonance frequency, this causes a dip in the transmission spectrum, an example is shown in figure 2.2. The sharpness and depth of this dip are captured in the Q-factor. The narrower and deeper the dip, the higher the Q-factor.

The Q-factor is defined as follows:

$$Q = \omega_0 \cdot \frac{E_{stored}}{P_{lost}}, \tag{2.3}$$

with ω_0 the resonance frequency, E_{stored} the electric and magnetic energy that is stored in the resonator per cycle and P_{lost} the power that is lost per cycle, higher loss implies lower Q and vice versa. Power can either be lost by intrinsic dissipation or through the coupler bar. The total (or loaded) quality factor is then given by:

$$\frac{1}{Q} = \frac{1}{Q_i} + \frac{1}{Q_c} \tag{2.4}$$

In this formula Q_i is the intrinsic Q-factor and Q_c the coupling Q-factor depending on the capacitance of the coupling [4].

2.4.2 Transmission

The transmission, the ratio between the voltage before and after the KID, $S_{21} = V_{out}/V_{in}$ is given by:

$$S_{21} = \frac{\frac{Q_l}{Q_i} + 2i\frac{\delta\omega}{\omega_0}}{1 + 2iQ\frac{\delta\omega}{\omega_0}}, \tag{2.5}$$

with $\delta\omega = \omega - \omega_0$, but can also be written as

$$S_{21} = 1 - \frac{Q_l/Q_c}{1 + 2iQ_l\frac{d\omega}{\omega_0}}. \tag{2.6}$$

Further derivations on S_{21} transmission can found in Refs. [8],[4] and [3]. S_{21} transmission at resonance gives a real, minimal value $S_{21,min} = Q/Q_i$. In a plot of the complex and imaginairy part of S_{21} you get a resonance circle. The resonance cirkle has a diameter of $1 - |S_{21,min}|$ and its center is at

$$r_c = \frac{1 + |S_{21,min}|}{2} = \frac{1 - \frac{Q_l}{Q_i}}{2}. \tag{2.7}$$

From these equations Q_c can be determined as follows

$$Q_c = \frac{1}{1 - S_{21,min}}Q \tag{2.8}$$

In reality, the dips can be asymmetric due to mismatched readout lines. This causes the resonance circle to rotate by angle ϕ and grow by a factor $1/\cos(\phi)$. In Ref. [6] this assymetry is described with a complex coupling quality factor $\hat{Q}_e = |Q_e|e^{i\phi}$ and a factor $(1 + \hat{\epsilon})$ [6]. The transmission is then given by:

$$S_{21} = (1 + \hat{\epsilon})(1 - \frac{Q_l/\hat{Q}_e}{1 + 2iQ_l\frac{d\omega}{\omega_0}} \tag{2.9}$$

ϕ is given by

$$\phi = \arctan(2Q\frac{\delta\omega}{\omega_0}) \tag{2.10}$$

in which $\delta\omega = \omega_1 - \omega_0$, see figure .2.3. Accurate extraction of Q-factors requires to correct for this asymmetry.

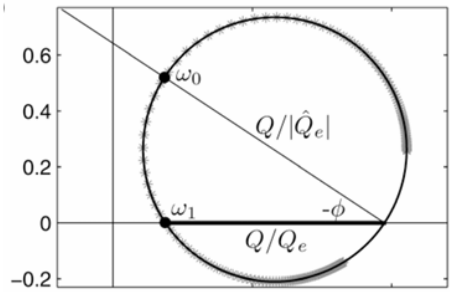

Figure 2.3: An example of a shifted resonance circle. The horizontal axis represents $Re(S_{21})$ and the vertical axis $Im(S_{21})$[6]

2.4.3 Scatter

The problem that is at the root of this thesis is the observed variation from designed Q-factors compared to measured Q-factors; Q-scatter. The fractional Q-scatter in either Q_c or Q_l is given by:

$$Q_{frac,l/c} = \frac{Q_{l/c} - Q_{design}}{Q_{design}}, \tag{2.11}$$

The main goal of this thesis is to find out the causes of Q-scatter in KID arrays. Below several hypotheses on the possible sources of Q-scatter will be introduced.

Design: The arrays are designed to have a uniform frequency spacing as well as a constant Q-factor of 5×10^4. These designs are based on SONNET simulations, but were done only for one single KID, not for a whole array. Therefore, the design doesn't take into account the possible effects of bridges or parasitic capacitances. Also, a fully working device is placed in a box, this can lead to more parasitic capacitors influecing Q-factors.

Fabrication: Uncertainties in the dimensions of the coupler bar, IDC or inductor can vary the resonance frequencies of a KID. These uncertainties may also effect the Q-factors.

Variations in Q_i: Q_i is dependent on losses inside the resonator. These losses are due excess quasi-particles, dielectric losses, hot phonon losses or other resonator impurities [10] [5]. These variations in Q_i may have influence on Q_c as well.

Electromagnetic coupling or crosstalk: As the KIDs are packed relatively close together, the electric or magnetic field inside a KID might influence its neighbours. Simulations in Ref. [14] shows Q-factors are impacted by crosstalk. The crosstalk decreases for increasing dF, where dF is the frequency difference between two neighbouring resonators.

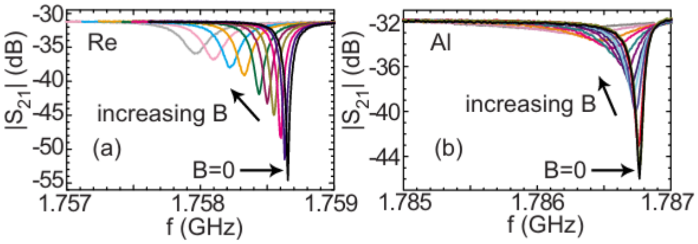

Figure 2.4: Dips plotted for different magnitudes of magnetic field. Both Re (left) and Al (right) show that both the resonance frequency as well as the Q-factor decrease as the magnetic field increases [12].

Transmission line effects: The transmission line couples all KIDs together, one defect in this component can thus influence the whole array. This can for example happen through the bridges, which are located every 150 μm evenly along the array. There is a possibilty that if the input and output impedances of KIDs are not be matched properly, not all the power is transmitted and a standing wave will be formed inside the transmission line. Another possibilty is that the transmission line is unbalanced due inappropiate grounding. Some KIDs would then receive either more or less power than initiated, resulting in a non-reprensentative S_{21} transmission, which could then give rise to Q-scatter.

Magnetic vortices: Superconductors expell an external magnetic field completely; the Meissner effect. However, thin-film type II superconductors in a magnetic field above a certain threshold allow some flux to get trapped in the superconducting material. These quantized filaments of flux are called vortices. Inside these vortices the material is not superconducting anymore and to shield the surrounding superconducting material, currents flow around the vortices. The amount of vortices in a material is dependent of the width of the strip and the applied external field, several studies where done on this relation including Refs. [13], [2] and [12]. When an external current is applied to the superconductor, the Lorentz force will move these vortices around, dissipating energy. As energy is dissipated this lowers both the resonance frequency and the Q-factor, making it a possible source of Q-scatter. In figure 2.4 the shift in Q-factor and resonance can be seen.

Chapter 3

Method

In this chapter is explained how the different properties of each chip are used to investigate the origin of Q-scatter. First, the fabrication method is discussed after which the difference in the KID devices will be explained. Lastly, we will discuss how the data was collected and analyzed.

3.1 Fabrication

The chips are made using lithography, a process where a wafer consisting of different layers is radiated leaving behind only an intented pattern. The wafer used for KID arrays relevant to this thesis are made from sapphire and have a diameter of 100 mm and thickness of 350 µm. First, a layer of either NbTiN or β-Ta is deposited across the entire substrate, which consists of a sapphire wafer. A photoresist layer is then spin-coated over the metal, uniformly covering the wafer. When exposed to light, the photoresist undergoes localized chemical changes that alter its solubility. A mask, designed according to the desired array pattern, ensures that only specific regions of the wafer are illuminated. Following the exposure, the wafer undergoes a development process in which the light-sensitive, now-soluble portions of the resist are removed, revealing the underlying metal. Reactive ion etching (RIE) is then used to selectively remove these exposed metal areas. Sulfur hexafluoride (SF_6) serves as an etchant, reacting with and removing the unwanted metal. Finally, the remaining, unexposed photoresist is stripped away, and the wafer is thoroughly cleaned. The result is a sapphire substrate with a precisely defined structure corresponding to the designed array[11].

The difference between optical and electron beam lithography is the radiation source. For optical lithography UV light is used, while electron beam lithography uses electrons, as the name might suggest. This difference then causes a difference in accuracy. This can be seen in figure 3.1 where the sides and corners are considerably sharper for ebeam lithography.

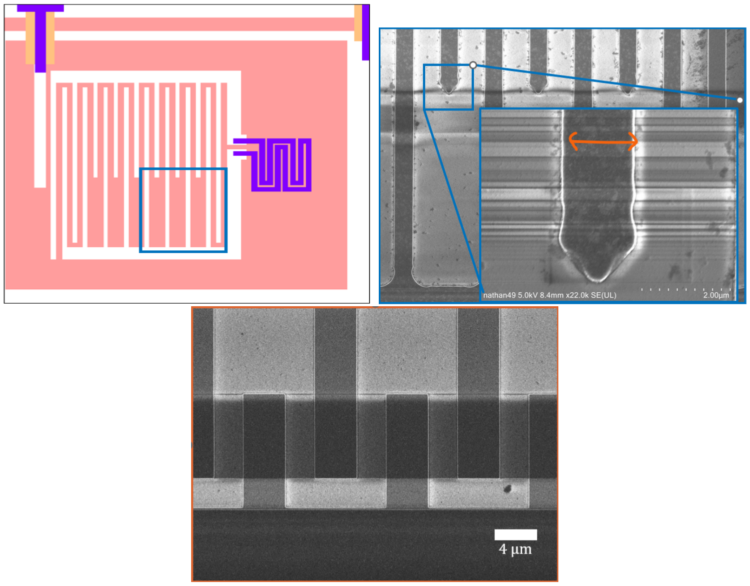

Figure 3.1: (Left) A representation of a KID, with the blue square zoomed in for both optical (right) and ebeam lithography (down).

3.2 KID devices

In order to find out what causes the Q-scatter several chips where used, with each different designs, differing in pixel count, spacing and fabrication. LT295 chip 3 is a 400 pixel chip made using optical lithography. LT361 chip 4 is a 400 pixel chip as well, but made using electron beam pattern generation (ebeam lithography). LT361 chip 7 has 121 pixels and is also made using ebeam lithography, but with more spacing in between the KIDs compared to the other chips. The chips will simply be referred to as chip 3, chip 4 and chip 7 respectively in the remainder of the report. Both chip 4 and 7 have a Q_{design} of 5.0×10^4 and a varying coupler bar, while for chip 3 the coupler bar is kept constant and the Q-factor is designed at 2.0×10^4. The goal of varying the coupler bar was to keep the Q-values constant. Unfortunately, this didn't work out, but it shows Q-scatter is worth investigating. A table that gives an overview of all the properties is given in table 3.1. The differences between the chips are visualized in figure 3.2.

By comparing chip 3 and 4 insights can be obtained whether or not the fabrication or the design are sources of Q-scatter. This will be done by comparing the standard deviations of their measured Q-factors. For chip 4 also data after trimming of the IDC-fingers to reduce frequency scatter as described in Ref. [11] was available, this chip will be called chip 4 trim. By comparing data of chip 4 before and after trimming, it's possible to check what influence trim-

	Chip 3	**Chip 4**	**Chip 7**
Type	NbTiN/b-Ta on Sapphire	NbTiN/b-Ta on Sapphire	NbTiN/b-Ta on Sapphire
pixels	400(20x20)	400(20x20)	121(11x11)
Pixel pitch (µm)	150	150	450
Lithography	Optical	Ebeam	Ebeam
Q_{design}	2×10^4	5×10^4	5×10^4
Coupler bar	Fixed	Varies with frequency	Varies with frequency

Table 3.1: A table with all the different properties of the chips

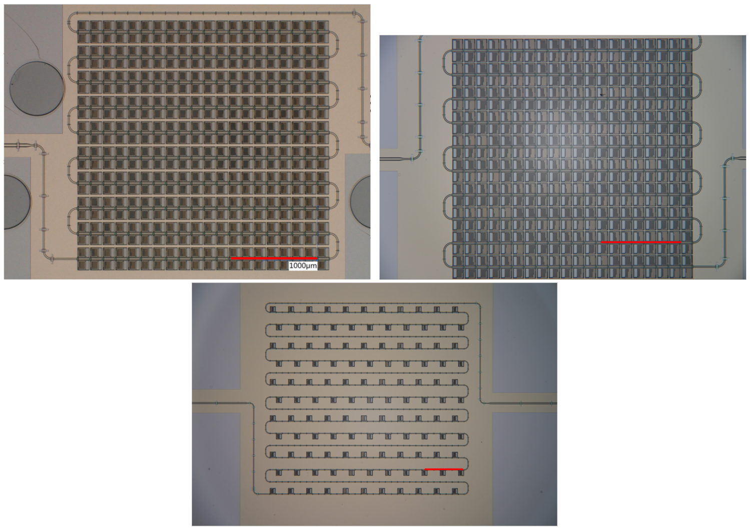

Figure 3.2: (Left) chip 3 and (right) chip 4 with the KIDs closely spaced and (down) chip 7 with more space in between the KIDs. The red line in each figure represents 1000 µm

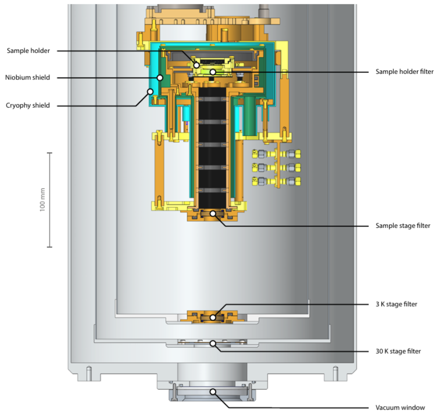

Figure 3.3: The cross-section of the used cryostat [9].

ming the IDC-fingers and an extra fabrication step have on the Q-factors as well.

Chip 4 and 7 differ in spacing between KIDs, allowing to see how electromagnetic coupling between KIDs might have impact on the Q-scatter. Furthermore, the larger spacing between the KIDs allows us to look at the impact of vortices. Vortices are more likely to form in larger spaces of ground plane as described in Ref. [13]. If chip 7 has higher Q-scatter this could indicate that vortices give rise to Q-scatter. By calculating the asymmetry parameter ϕ with equation (2.10) a closer look to mismatched impedances can be taken. This also allows to see if a standing wave is formed in the transmission line, if this causes asymmetric dips.

3.3 Cryogenic measurement setup

Superconducting detectors require temperatures below their critical temperatures T_c, because only then Cooper pairs are formed. The critical temperature of β-Ta is 1.0 K [9]. Measurements were performed at a temperature of $T \sim T_c/10$. To achieve such low temperatures a Bluefors Helium dilution cryostat, shown in figure 3.3, was used. This cryogenic environment ensures stable operation well below T_c, minimizing thermal quasiparticle generation and enabling single-photon sensitivity.

3.4 Measuring and mapping Q

Once the chip is sufficiently cooled down, a VNA scan is performed to measure the S_{21} transmission spectrum across a frequency range of 4-6 GHz for chip 3 and 4-8 GHz for the other two chips as seen in figure 3.4. These scans are performed using LabVIEW and capture both the amplitude and phase of the

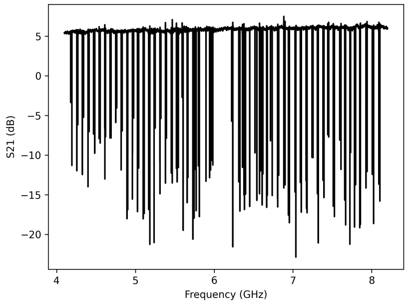

Figure 3.4: The data obtained after performing a VNA scan on LT361 chip 7.

signal. At each resonance frequency a dip appears in the amplitude accompanied by a phase shift. The exact shape and depth of these dips encode information about the loaded, internal, and coupling Q-factors of each resonator. Thus each dip in figure 3.4 has a corresponding Q-factor, the parameter in which we are interested in this thesis. The calculation of the Q-factors is briefly described in section 2.4 and extensively by K. Kouwenhoven in his PhD dissertation [8]. A Python code was made based on Ref. [6].

The correspondence between resonance frequencies and their respective KIDs is established as described in Ref. [11]. The calculation of the Q-factor is done independently of the resonance frequency. Therefore, a Q-factor is not directly coupled to its corresponding KID. However, by using the known mapping between resonance frequency and KIDs, the Q-factors can be indirectly assigned to the correct KID, for this a Pyhton script was made. Once the Q-factors were calculated and coupled to the right KIDs, plots were made of mainly Q_c. These plots, made to investigate for any relationships in the data, include histograms, heatmaps and scatter plots.

3.5 Power

Looking at the data, we observe that Q-factors vary for the different powers that are sent through the transmission line. Therefore, before analyzing and comparing Q-factors of different chips, we check which power gives the most representable Q-values. In figures 6.1, 6.2, 6.3 and 6.4 in the Appendix for each KID device dips of a representative KID are shown for four powers (-100 dBm, -108 dBm, -116 dBm and -120 dBm). Powers below -90 dBm give non representative dips and fits, so only powers form -100 dBm and above are shown. Looking at figure 3.5, Q-factors converge towards their design value as power decreases. A power of -116 dBm shows the most stable behaviour and smallest errorbars, this also accounts for chip 3. Therefore, we take this power as representative and use the corresponding data for analyzing.

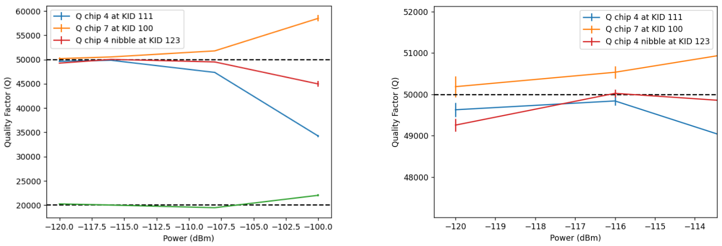

Figure 3.5: Errorbar plot of the Q-factors from a representative KID from each of the KID devices. Left shows how the Q-factors converges to its design values and right is a zoomed in plot which shows the errorbars are smallest for -116 dBm.

Chapter 4

Results and discussion

In this chapter we will discuss the results obtained after analyzing the data. First, we take a global look at the data after which we dive deeper into the scatter data by checking and comparing different parameters. Lastly, we will take a look at what trimming does to the Q-scatter.

In figure 4.1 the values for all Q-values are plotted on a log-scale against their corresponding frequencies. Values for which Q_c is bigger than 1.5×10^5 are considered unrepresentative looking at the fits of their dips. The same accounts for Q_i-values below 1×10^5 and above 2×10^6. We can see that $Q_i >> Q_c$, which makes $Q_l \approx Q_c$ an appropiate approximation considering equation 2.4. For all chips account that the Q_c-values decrease with increasing frequency. For this relationship a $1/\omega^2$-fit, based on Ref. [4], was made. The fit can be seen in the figure as the red dashed line.

Looking at figure 4.1, the observed frequency effect is very inlikely to be due fabrications errors. The thickness of the metals on the wafer slighty varies across the array. If that variation would play a dominant role, you would observe a spatial effect as certain parts of the chip would systematically differ. However, as frequencies are spread all over our chip and no such spatial effect is observed, it makes it very unlikely fabrication is a cause of Q-scatter.

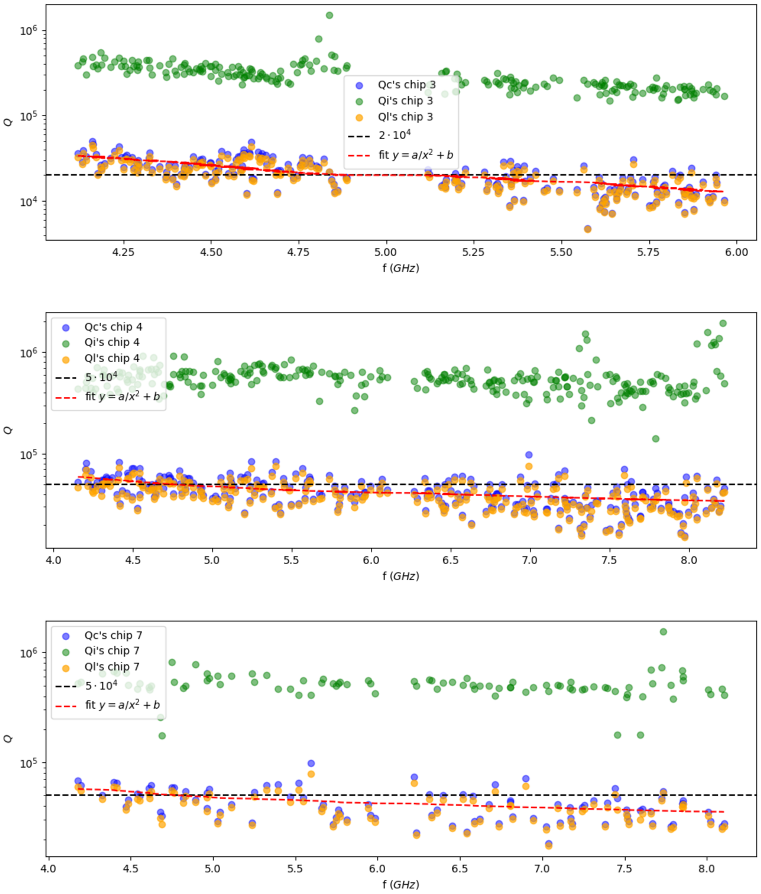

Figure 4.1: Scatter plots for the Q-values for all chips with the black dashed line being the designed values. In red is the fit relation.

4.1 Scatter

The scatter in Q_c for each chip is visualised in the histograms in figure 4.2. The fractional Q_c was calculated using equation (2.11) in section 2.4.3, where different Q_{design}-values were taken. The corresponding mean and standard deviations can be found in table 4.1. The column with '$1/\omega^2$' means the Q_{design}-values are the Q-values extracted from the fit in figure 4.1 to account for the frequency effect. In the column with 'simulations' the fractional Q_c was calculated using simulations values. For chip 4 and chip 7 these simulations values are simply 5×10^4, as for these chip the coupler bar was varied to keep the Q-factor constant. The Q-factors for chip 3 were origally designed to be 2×10^4. However, in the design the coupler bar was not varied leading to simulated Q_c-factors

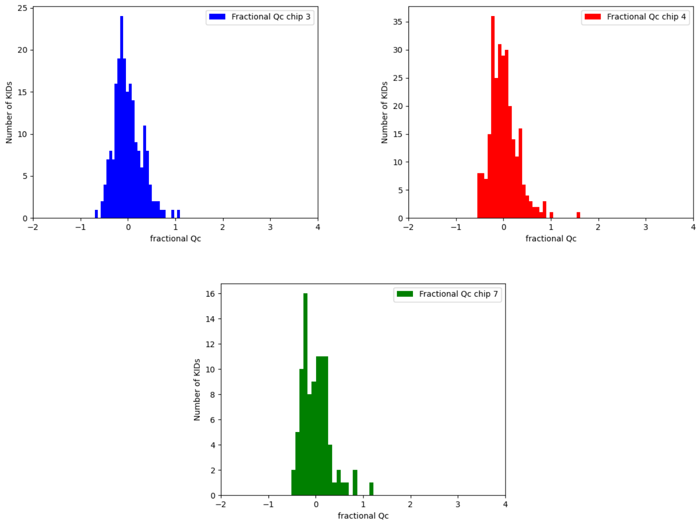

Figure 4.2: Histograms of the fractional Q_c-scatter for the three chips with Q_{design} being the $1/\omega^2$-values.

that deviated from this value. To extract correct simulation values, simulations using Sonnet where performed. The last column shows the fractional Q_c given a constant Q-factor of 2×10^4 and this only accounts for chip 3.

First, we take a look at the first column in which the fractional Q_c is calculated using the $1/\omega^2$-values. As can be seen in the table the values are very much alike, with the standard deviation being 0.30 for chip 3 and chip 7 and 0.29 for chip 4. From this we can conclude that the more accurate fabrication using ebeam lithography has no influence on the Q-scatter. Then looking at the second column, we see similar values for chip 4 and chip 7, but a slightly higher value for chip 3. Also, the fractional Q_c for chip 3 taken a constant Q-factor of 2×10^4 is a significantly higher compared to 0.28. This indicates that varying the coupler to keep a constant Q-factor does slightly decrease the Q-scatter. However, as the standard deviation still remains 0.28 for both chip 4 and chip 7, this can not be assigned the origin of Q-scatter.

Now, we take a closer look at the values for chip 4 and chip 7. As chip 7 has a larger spacing between KIDs, a difference in Q-scatter could have given some clues on whether electromagnetic coupling or vortex forming played a role in Q-scatter. The bigger spacing in chip 7 could have reduced the electromagnetic coupling, but could have also caused more vortex forming. However, all values for chip 4 and 7 are very similar indicating both possible causes are unlikely to impact Q-scatter. We know from Ref. [14] that crosstalk is only present between two neighbouring KIDs with small differences in resonance fre-

Device	$1/\omega^2$		Simulations		2×10^4	
	μ	σ	μ	σ	μ	σ
Chip 3	2.9×10^{-2}	0.30	30×10^{-2}	0.38	8.3×10^{-2}	0.43
Chip 4	0.95×10^{-2}	0.29	-15×10^{-2}	0.28	-	-
Chip 7	0.55×10^{-2}	0.30	-15×10^{-2}	0.28	-	-

Table 4.1: The mean and standard deviation values for the different fractional Q_c-values for all chips.

quencies. The designs for both chip 4 and 7 are such that spatial neighbours have a sufficiently large resonance frequency difference, making electromagnetic coupling unlikely from the beginning. Moreover, the simulations from Ref. [14] show that due crosstalk the Q_c of one the KIDs peaks, while the other slowly dips. This would result in a histogram with two separate branches, but this is not apparent in either histogram, excluding crosstalk to be a source. Another implication that can be made from the histograms, is that vortices are unlikely to be a source of Q-scatter source as well. Since the environment around each KID in chip 7 is similar, vortices would all have the same influence on the KIDs, resulting in a constant shift from its design values. However, looking at the histogram of chip 7, this shift is not observed.

4.1.1 Spatial dependence

To investigate potential spatial trends in Q-scatter, spatial plots were generated mapping Q_c across each chip. Every square represents a KID, KIDs that could not be coupled by frequency or had non representative Q-values are shown in white. For chip 3 frequency neighbours were spatial neighbours as well, resulting in quite some unmatched KIDs. Keep in mind that chip 7 has larger spacing between the KIDs, see figure 3.2.

Looking at the spatial plots in figure 4.3 no specific effect is observed. Although you could say that KIDs that could not be coupled, are somewhat clustered. To check for any tranmission line effects, the spatial plots were flattened out. This way the fractional Q-scatter, using the $1/\omega^2$-values, can be plotted as a function of distance along the transmission line in figure 4.4. Bridges are present every 150 µm along the transmission line, but there seems to be no effect that influences the Q-scatter that can be assigned to these bridges. The periodicity for chip 7 is due the design of chip 7 where some parts of the transmission line are not connected to any KIDs as can be seen in figure 3.2.

No observed relation between transmission line and Q-scatter does not directly mean bridges or other transmission line properties have no effect at all. To check for other relations, the asymmetry along the transmission line is investigated. The asymmetry of the dips is captured in parameter ϕ, introduced

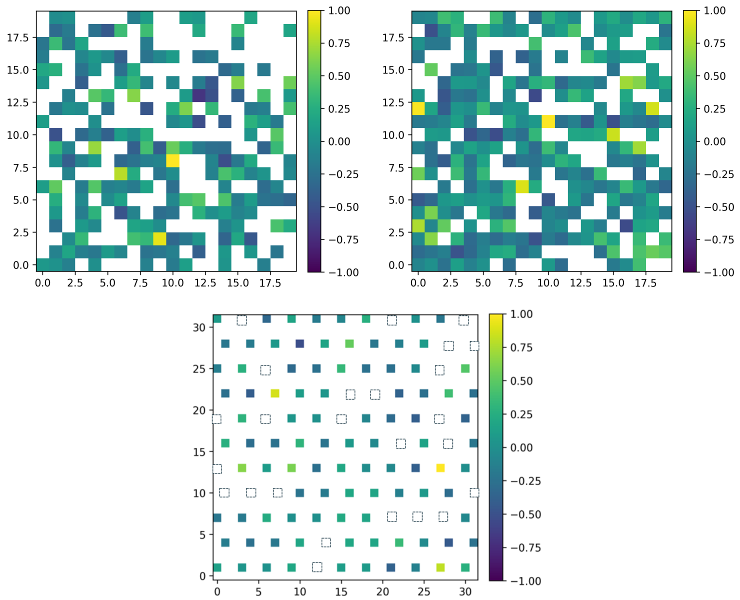

Figure 4.3: Spatial plots of the fractional Q_c for chip 3 (upper left), chip 4 (upper right) and chip 7 (lower right). The colorbars on the right show the corresponding values to the colors.

by Ref. [6], according to formula (2.10). The asymmetry could be affected by its position on the chip through either mismatched in- and output impedances forming standing waves or inappropiate grounding. For this analysis ϕ is plotted against distance along the transmission line in figure 4.5.
As can be seen in the figure, ϕ does not show any spatial or periodic effect that would indicate any spatial dependence. Chip 3 seems to show slightly higher ϕ values further up along the transmission line. This could be a result of less accurate fabrication using optical lithography, where reflections of the signal cause more asymmetry. Since the overall scatter in chip 3 is similar to chips 4 and 7, this could point out that asymmetry is correctly accounted for by Ref. [6] and has no influence on the Q-scatter. Again, the periodicity for chip 7 is due its design.

4.2 Correlations

To check if Q-scatter isn't due to scatter in Q_c itself, but maybe due changes in Q_i or ϕ, we check their correlations. The Pearson correlation values between Q_c and Q_i, and Q_c and ϕ for each chip are calculated using Python and can be found in table 4.2.
Chip 4 and 7 have a similar coefficient with 0.12 and 0.15 respectively, while the correlation for chip 3 is slightly higher with 0.41. Although all the Q_c/Q_i-

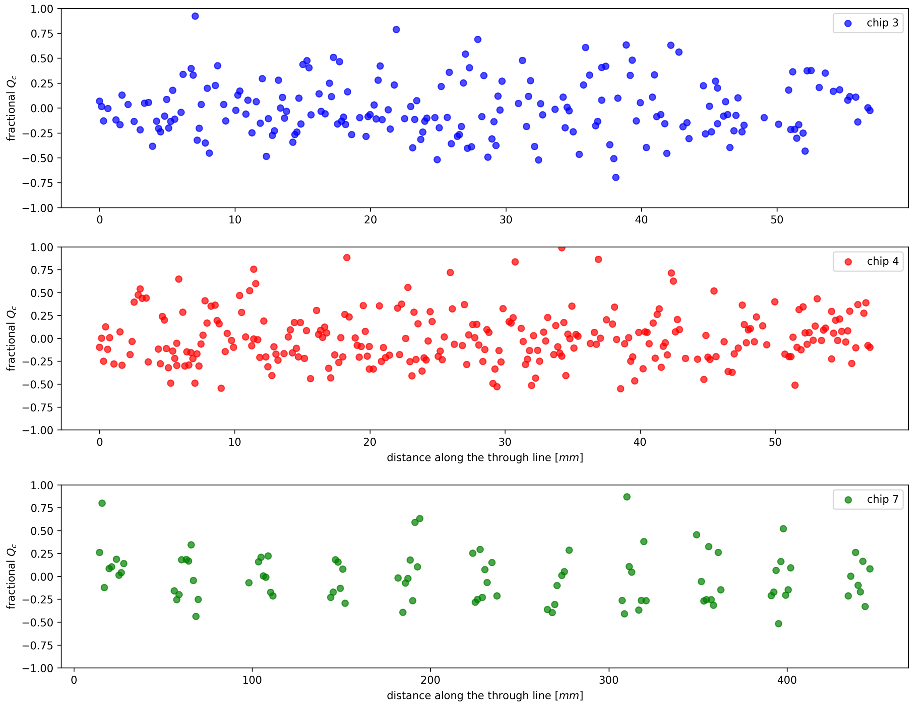

Figure 4.4: The fractional scatter of Q_c plotted against the distance along the transmission line.

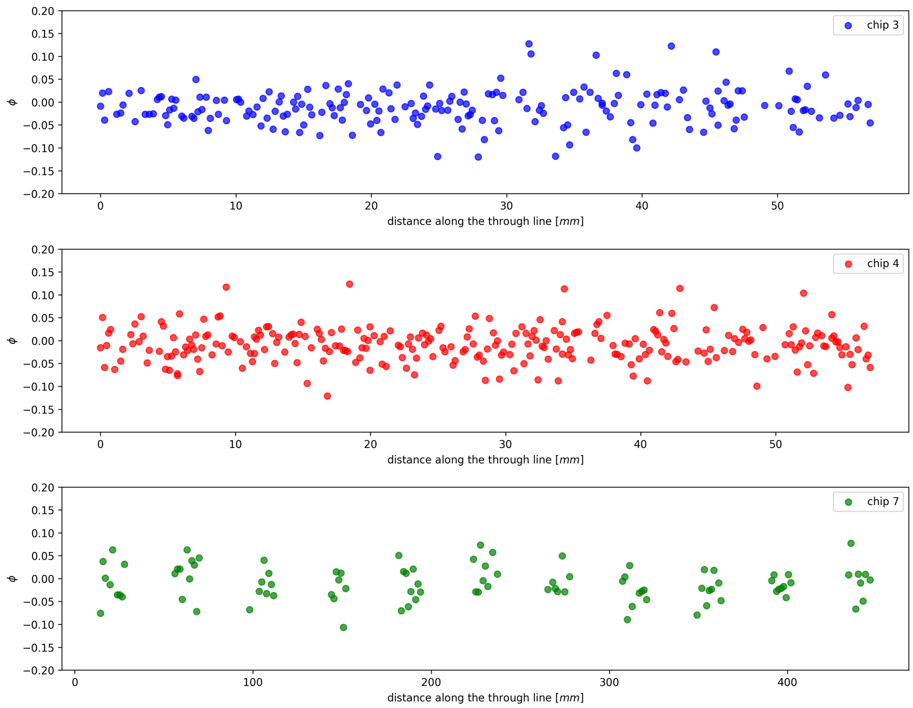

Figure 4.5: Asymmetry parameter ϕ plotted against the distance along the transmissin line.

correlations are positive, meaning a higher Q_c gives a higher Q_i or vice versa, the coefficients are too low to draw conclusions. A plot where the fractional Q_c is plotted against the asymmetry of the dips is given in figure 4.6. Larger ϕ-values do not neccesarily correspond to higher scatter values and also the correlation values for this correlation are too low to speak of any relationship between Q_c and ϕ. Again, we can concluded asymmetry is correctly treated in Ref.[6] and does not contribute to Q-scatter.

	Correlation Q_c and Q_i	Correlation Q_c and ϕ
Chip 3	0.41	0.09
Chip 4	0.12	0.15
Chip 7	0.15	-0.10

Table 4.2: The correlation coefficients between Q_c and Q_i and Q_c and ϕ for each chip.

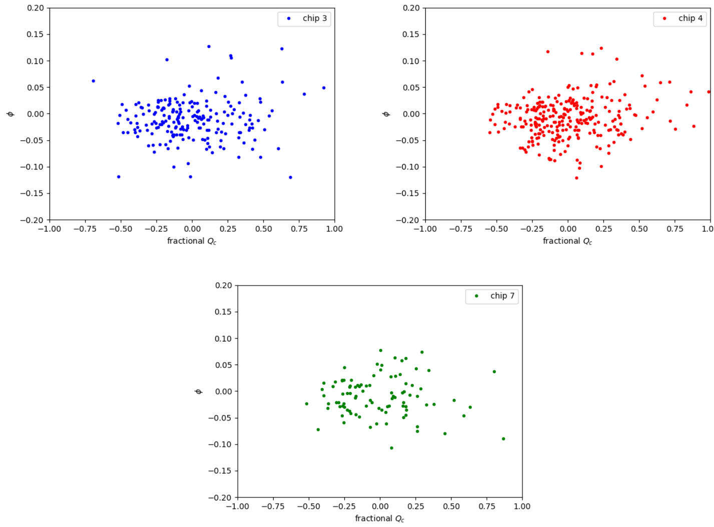

Figure 4.6: The fractional scatter of Q_c plotted against asymmetry parameter ϕ.

4.3 Trim comparison

To gain insights into how trimming the IDC-fingers influence Q-scatter, we also take a look into the data of chip 4 after trimming and compare this with the values of chip 4 before the trimming.

The histogram of chip 4 after trimming is given in figure 4.7. The different Q-scatter values for chip 4 after trimming are given in table 4.3. The slightly higher standard deviation compared to the pre-trim data, although it doesn't

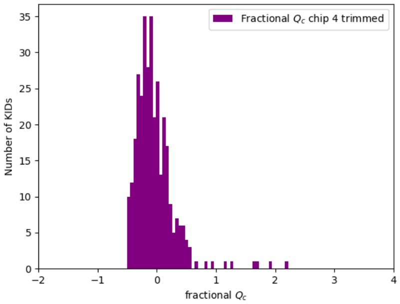

Figure 4.7: The histogram of the post-trimming Q-scatter of chip 4 using the $1/\omega^2$-values.

Device	$1/\omega^2$		Simulations	
	μ	σ	μ	σ
Chip 4 trim	3.9×10^{-2}	0.34	-14×10^{-2}	0.31

Table 4.3: The mean and standard deviation values for the different fractional Q_c-values for chip 4 after trimming.

change the Q-scatter significantly, can be due the extra fabrication step required to trim the IDC-fingers or by changing the IDC-fingers itself. However, a control group was taken in the experiment in Ref. [11] where the fingers of the first 80 KIDs were not trimmed and thus only exposed to the extra fabrication step. As these KIDs are scattered just as much as the others, the changing of the IDC-fingers itself can be ruled out.

Taking a closer look at the Q-values for chip 4 before and after trimming we see an interesting fact. Although the trend is the same, there is a significant difference in the Q-values before and after trimming as can be seen in figure 4.8. In figure 4.9 a histogram of the difference between the Q_c's is given and a mean of -0.9×10^3 and a standard deviation of 12.2×10^3 are found. If the Q_c-values had remained the same or at least stayed close together, it would have indicated that trimming had no influence on Q_c. However, given this relatively large standard deviation it is indicated that Q_c is scattered all over again after trimming.

As said before, it is very unlikely this new scattering is caused by changing the length of the IDC-fingers as a control group that was not trimmed shows new scattering as well. Also, the consequences of the extra fabrication step are impropable to be to cause of the new scattering. In section 4.2 we already checked for a correlation between Q_i and Q_c and no significant correlation was found, making it improbable a change in Q_i would the influence Q_c and cause the new scatter.

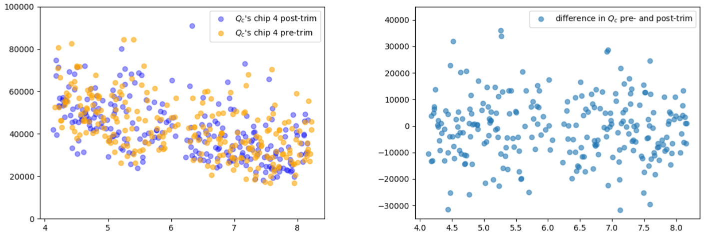

Figure 4.8: (Left) The Q_c-values of chip 4 before and after trimming against the corresponding resonance frequency. (Right) The difference between the Q_c-values against the corresponding frequencies.

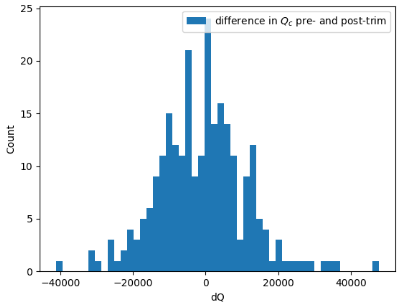

Figure 4.9: The histogram of the difference between Q_c's.

What remains as a possible source of the new scattering is the measuring of the chip itself. When measurements are performed on a chip, the chip is mounted in the cryostat and wired in order to get a signal through the tranmission line. After the measurement, the chip is warmed up again and demounted from the cryostat before it is mounted and cooled down again for a following measurement. As this is the only further difference between chip 4 before and after trimming the new scatter should be due of one these steps, by for example the formation on new parasitic capacitances as the chip is remounted of rewired. Based on the experiments conducted for this thesis it is not possible to give a concrete cause of this new scattering. To gain more insights in the new scattering more simulations and experiments are needed.

Chapter 5

Conclusion

In this thesis, we studied the origin of Q-scatter in arrays of superconducting kinetic inductance detectors (KIDs). Three chips with different fabrication methods, pixel spacing and pixel count were analyzed and compared by several parameters extracted from their S_{21} data.

The analysis showed Q-scatter is not impacted by using the more accurate ebeam lithography comparded to optical lithography. Comparing chip 3 and 4, it is indicated that varying the coupler bar does slighty decreases Q-scatter, but it does not fully eliminates it. Looking at the data from chip 4 and 7 we can conclude both electromagnetic coupling and vortex forming are very unlikely to be a cause of Q-scatter as well. Spatial plots showed no evidence that for example bridges have effect on Q-scatter. More specifically, no effect was observed that suggested any dependency of transmission line effects on the Q-scatter. Furthermore, no significant correlations between Q_c, Q_i and ϕ, that could point to the origin of Q-scatter, were found. Lastly, the difference in Q-scatter before and after trimming chip 4 were investigated. Although, scatter values were similar, the Q-factors per KID showed large deviations. This suggested that the Q-factors are scattered all over again after trimming. As the trimming of the IDC-fingers itself is very unlikely to be a source of Q-scatter, this new scatter is more likely to be caused by other things than the chip itself. Mounting, wiring and cooling down the chip which then forms parasitic capacitances belong to the possibilties of where this new scattering or the scatter in general finds its origin.

This thesis has showed that design, fabrication method, electromagnetic coupling, vortex forming, transmission line effects or any relation between Q_c, Q_i and ϕ are unlikely to be the or a source of Q-scatter. In order to give a full explanation of where Q-scatter originates from, more experiments are required, beginning with simulations. With the newly published version of Sonnet (v19), simulations such as those performed in [14] can be scaled to complete array dimensions. Also, more experiments need to be performed that give more insights in the newly scattered Q-factors of chips in different measurements.

Chapter 6

Appendix

The dips and their fit to check for which power the fit and thus Q-factor are the most representative.

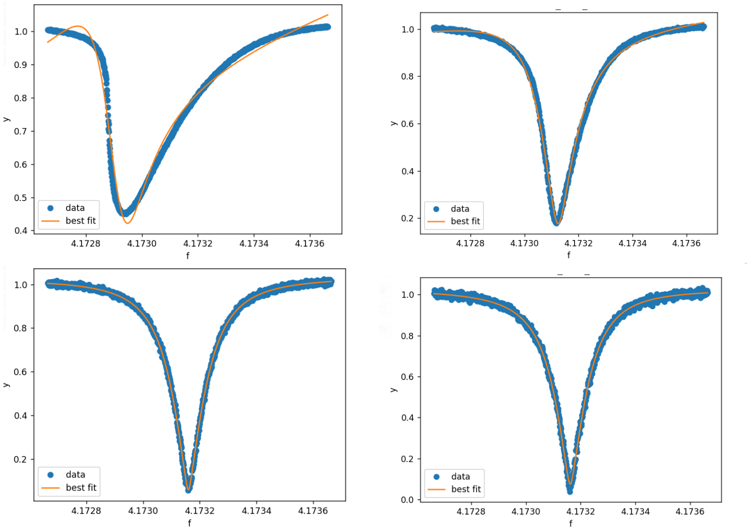

Figure 6.1: transmission dip of KID 12 of chip 3 at a power of -100 dBm (upper left) with $Q = 2.20 \times 10^4$, -108 dBm (upper right) with $Q = 1.94 \times 10^4$, -116 dBm (lower left) with $Q = 2.00 \times 10^4$ and -120 dBm (lower right) with $Q = 2.03 \times 10^4$. The dip converges to a constant shape as the power decreases.

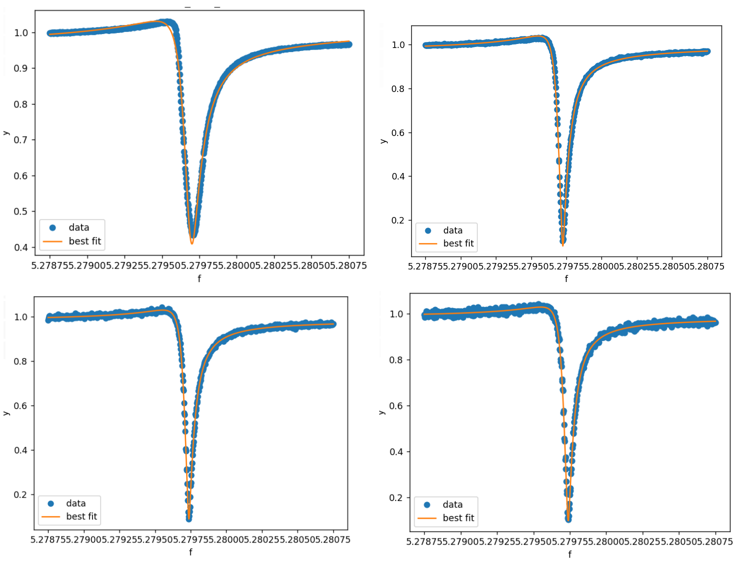

Figure 6.2: Transmission dip of KID 111 of chip 4 at a power of -100 dBm (upper left) with $Q = 3.42 \times 10^4$, -108 dBm (upper right) with $Q = 4.73x10^4$, -116 dBm (lower left) with $Q = 4.98 \times 10^4$ and -120 dBm (lower right) with $Q = 4.96 \times 10^4$. The dip converges to a constant shape as the power decreases. For all dips a resonance frequency of 5.279 GHz was found.

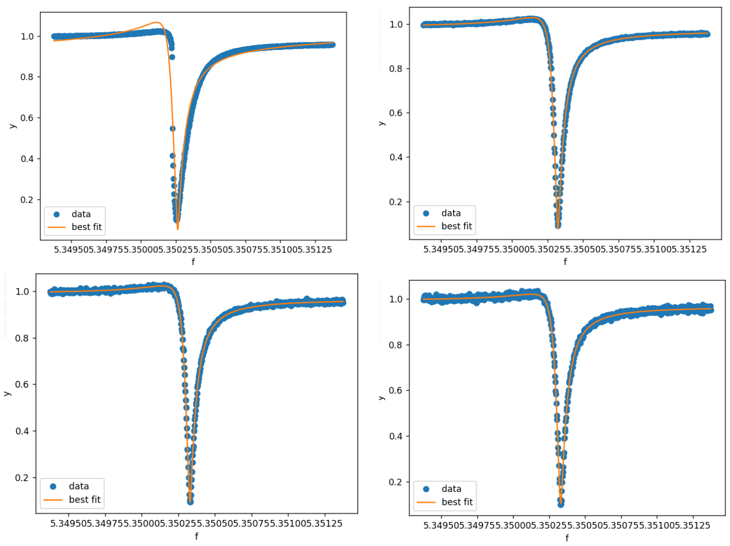

Figure 6.3: Transmission dip of KID 123 of chip 4 nibble at a power of -100 dBm (upper left) with $Q = 4.50 \times 10^4$, -108 dBm (upper right) with $Q = 4.95x10^4$, -116 dBm (lower left) with $Q = 5.00 \times 10^4$ and -120 dBm (lower right) with $Q = 4.92 \times 10^4$. The dip converges to a constant shape as the power decreases. For all dips a resonance frequency of 5.350 GHz was found.

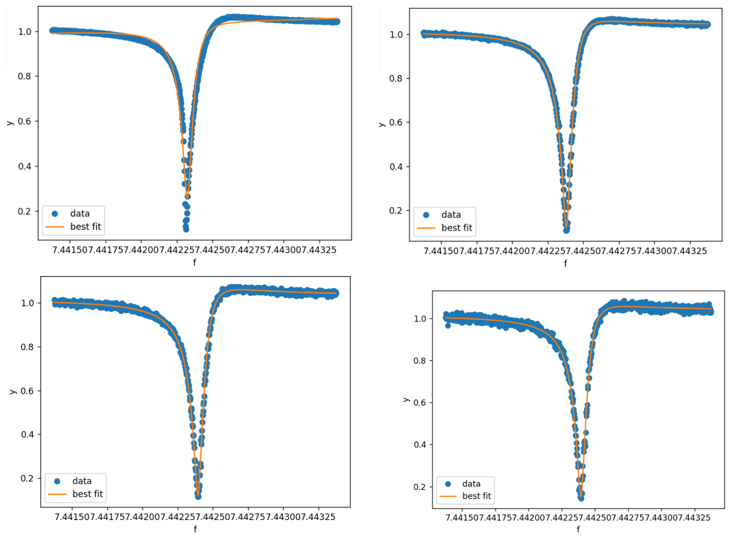

Figure 6.4: Transmission dip of KID 100 of chip 7 at a power of -100 dBm (upper left) with $Q = 5.85 \times 10^4$, -108 dBm (upper right) with $Q = 5.18 \times 10^4$, -116 dBm (lower left) with $Q = 5.05 \times 10^4$ and -120 dBm (lower right) with $Q = 5.02 \times 10^4$. The dip converges to a constant shape as the power decreases. For all dips a resonance frequency of 5.279 GHz was found.

Bibliography

[1] Reading an Earth-like Exoplanet's Transmission Spectrum, May 2025.

[2] Ruiheng Bai, Aliakbar Sepehri, Yen-Lee Loh, Anne-Marie Valente-Feliciano, Anna Herr, Quentin Herr, and Katja C. Nowack. Flux trapping in NbTiN strips and structures, 3 2025.

[3] Rami Barends. *Photo-detecting superconducting resonators*. PhD thesis, Technische Universiteit Delft, 2009.

[4] Pieter de Visser. *Quasiparticle dynamics in aluminium superconducting microwave resonators*. PhD thesis, Technische Universiteit Delft, 2014.

[5] Alex Gurevich. Tuning microwave losses in superconducting resonators. *Superconductor Science and Technology*, 36(6):063002, 3 2023.

[6] M. S. Khalil, M. J. A. Stoutimore, F. C. Wellstood, and K. D. Osborn. An analysis method for asymmetric resonator transmission applied to superconducting devices. *Journal of Applied Physics*, 111(5), 3 2012.

[7] K. Kouwenhoven, I. Elwakil, J. Van Wingerden, V. Murugesan, D. J. Thoen, J. J. A. Baselmans, and P. J. De Visser. Model and Measurements of an Optical Stack for Broadband Visible to Near-Infrared Absorption in TiN MKIDs. *Journal of Low Temperature Physics*, 209(5-6):1249–1257, 7 2022.

[8] Kevin Kouwenhoven. *Visible to Near-Infrared Kinetic Inductance Detectors Energy-Resolving Single Photon Detectors*. PhD thesis, Technische Universiteit Delft, 2024.

[9] Kevin Kouwenhoven, Daniel Fan, Enrico Biancalani, Steven A.H. De Rooij, Tawab Karim, Carlas S. Smith, Vignesh Murugesan, David J. Thoen, Jochem J.A. Baselmans, and Pieter J. De Visser. Resolving Power of Visible-To-Near-Infrared Hybrid Ta/NbTiN Kinetic Inductance Detectors. *Physical Review Applied*, 19(3), 3 2023.

[10] C. R. H. McRae, H. Wang, J. Gao, M. R. Vissers, T. Brecht, A. Dunsworth, D. P. Pappas, and J. Mutus. Materials loss measurements using superconducting microwave resonators. *Review of Scientific Instruments*, 91(9), 9 2020.

[11] Hessel Schulte. Exploring the limits of multiplexing kinetic inductance detectros. Master's thesis, Technische Universiteit Delft, 2024.

[12] C. Song, T. W. Heitmann, M. P. DeFeo, K. Yu, R. McDermott, M. Neeley, John M. Martinis, and B. L. T. Plourde. Microwave response of vortices in superconducting thin films of Re and Al. *Physical Review B*, 79(17), 5 2009.

[13] Gheorghe Stan, Stuart B. Field, and John M. Martinis. Critical Field for Complete Vortex Expulsion from Narrow Superconducting Strips. *Physical Review Letters*, 92(9), 3 2004.

[14] S. J. C. Yates, J. J. A. Baselmans, A. M. Baryshev, S. Doyle, A. Endo, L. Ferrari, S. Hochgürtel, and B. Klein. Clean Beam Patterns with Low Crosstalk Using 850 GHz Microwave Kinetic Inductance Detectors. *Journal of Low Temperature Physics*, 176(5-6):761–766, 1 2014.